Coastal Engineering Journal

AN IMAGING TECHNIQUE FOR MEASURING WAVE SURFACE SHAPES

YASUNORI WATANABE
School of Engineering, Hokkaido University
North 13 West 8, Sapporo, 060 8628, Japan
yasunori@eng.hokudai.ac.jp

YUTA MITOBE
School of Engineering, Hokkaido University
North 13 West 8, Sapporo, 060 8628, Japan

KAORI OSHIMA
Dept. of Civil Engineering, Penta Ocean Construction Ltd.
Koraku 2-2-8, Bunkyo-ku, Tokyo, 112-8576, Japan

Received (Day Month Year)
Revised (Day Month Year)

A novel imaging technique for identifying the locations of free-surface shapes was applied to three-dimensional hydraulic tests of coastal structures. Three-dimensional wave fields, consisting of superposed local reflected and diffracted waves, were measured around a breakwater and the mouth of a model harbor in a laboratory wave basin, and the results are consistent with the predictions of a Boussinesq-type equation model. The new technique was applied to surf zone waves to describe the organized deformation of breaking wave faces that evolve during wave propagation. Typical finger-shaped jets form in the wake of plunging jets, and a local depression trails behind a breaking wave front.

Keywords: Wave shape; Imaging measurement; Projector.

1. Introduction

It is well known that breaker-induced vortices and turbulence near a free surface deform the surface locally, and thus the local surface shape reflects the turbulence structures (Brocchini and Peregrine 2001). The subsurface longitudinal counter-rotating vortices produced beneath breaking waves (Watanabe et al. 2005) entrain the surface into the inner fluid region to form a local depression trailing behind the breaking wave front (the so-called scars) (Watanabe and Mori 2008). These vortices also entrain both outer and inner surfaces of a overturning jet to laterally fragment the jet, resulting in the formation of finger jets (Saruwatari, Watanabe, and Ingram 2008). These correlations between subsurface flow and surface shape suggest that

quantification of the local surface shape is essential to understand the near-surface turbulence that evolves dynamically beneath breaking waves. However, single-point measurements via conventional wave gauges do not enable one to determine the features of these complex three-dimensional surfaces.

Also, in a laboratory wave experiment with model structures, a complex wave field is generally formed by superposition of incident, reflected, and diffracted waves, with diverse wave directions near the structure. While wave gauges are conventionally arrayed around the structures to measure the spatial distribution of the wave heights, technical difficulties in resolving the superposed waves into wave components from multiple wave records at discrete locations preclude identifying the spatial ranges of these waves. Accordingly, a reasonable technique with wide applicability to wave experiments is sought for measuring three-dimensional, free-surface shapes as an alternative to conventional wave gages.

We propose a new imaging technique for measuring free-surface shapes with a digital video camera and a PC projector. A color block pattern is projected into dye-imbued water by the PC projector, and the surface of the water is recorded by the digital camera using an experimental setup similar to that of Chen and Li (2003). Three-dimensional surface shapes are estimated on the basis of the recorded relative locations of the block projections on the surface. The technique was applied to three-dimensional hydraulic tests of a wave field with simple structures and to a breaking wave experiment.

This paper is organized as follows. The measurement algorithm, calibration procedure, and image processing technique are explained in Section 2. The equipment and procedures used for the three-dimensional hydraulic tests (conducted in a wave basin) and the breaking wave experiment (performed in a wave flume) are described in Section 3. In Section 4, the reliability and capabilities of the new technique are investigated by comparing the measured surface shapes around structures with the numerical predictions of a Boussinesq-type wave equation model. The evolution of local surface deformations in breaking waves is also discussed, including comparisons with previous research. The results are summarized in Section 5.

2. Algorithm

In the present method, a PC projector and digital video camera are used to measure three-dimensional locations on the surface of an object (Fig. 1). A square-block pattern (see Fig. 2) is projected from the PC projector to illuminate the object.

The object surface, where the block pattern is reflected, is recorded by the camera. The camera coordinate system (x_c, y_c, z_c), with its origin at $\boldsymbol{O_c} = (O_{cx}, O_{cy}, O_{cz})$ in the real reference frame (x_r, y_r, z_r), is defined as shown in Fig. 1: z_c is the optical axis normal to the focal image plane, and the orthogonal axes x_c and y_c are oriented in directions perpendicular to z_c.

The real coordinates are related to the image and projector coordinates via a conventional pin-hole model. Assuming a perspective transformation of the camera

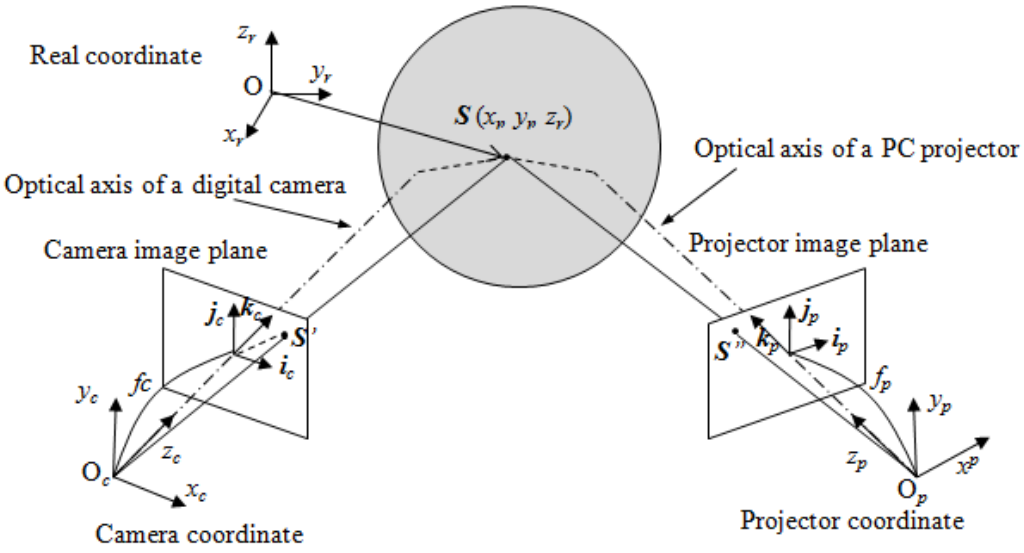

Fig. 1. Definition of image, projector and real-space coordinates.

coordinates, the image coordinates on the focal plane (x'_c, y'_c) can be expressed by

$$x'_c = f_c \frac{x_c}{z_c} \tag{1}$$

$$y'_c = f_c \frac{y_c}{z_c}, \tag{2}$$

where f_c is the focal length of the camera (distance between the focal plane and $\boldsymbol{O_c}$ along the optical axis). In this system, the object surface located at $\boldsymbol{S} = (x_r, y_r, z_r)$ is mapped to $\boldsymbol{S'}(x'_c, y'_c)$ in the image coordinate system via a perfect perspective transform, yielding the relations $\boldsymbol{S_c} = \overrightarrow{O_c S} = \boldsymbol{S} - \boldsymbol{O_c}$ and $\boldsymbol{S'_c} = \overrightarrow{O_c S'} = \boldsymbol{S'} - \boldsymbol{O_c}$:

$$\boldsymbol{S'_c} = \frac{f_c}{\boldsymbol{S_c} \cdot \boldsymbol{k_c}} \boldsymbol{S_c}, \tag{3}$$

where $\boldsymbol{k_c} = (k_{cx}, k_{cy}, k_{cz})$ is the unit vector normal to the camera image coordinates. Defining the orthogonal unit vectors $\boldsymbol{i_c} = (i_{cx}, i_{cy}, i_{cz})$ and $\boldsymbol{j_c} = (j_{cx}, j_{cy}, j_{cz})$ (perpendicular to $\boldsymbol{k_c}$) in the x'_c- and y'_c-directions of the image coordinate system, the location with image coordinates (x'_c, y'_c) can be written as

$$x'_c = \boldsymbol{S'_c} \cdot \boldsymbol{i_c} = \frac{f_c}{\boldsymbol{S_c} \cdot \boldsymbol{k_c}} \boldsymbol{S_c} \cdot \boldsymbol{i_c} \tag{4}$$

$$y'_c = \boldsymbol{S'_c} \cdot \boldsymbol{j_c} = \frac{f_c}{\boldsymbol{S_c} \cdot \boldsymbol{k_c}} \boldsymbol{S_c} \cdot \boldsymbol{j_c} \tag{5}$$

Substituting Equations (1) and (2) into the above equations, we obtain a system of

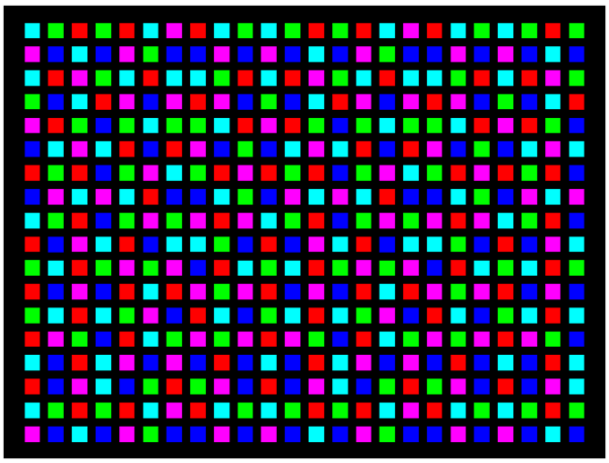

Fig. 2. An example of projecting color blocks whose neighboring colors are all different.

equations with respect to the real coordinates x_r, y_r and z_r:

$$x_r(x'_c k_{cx} - f_c i_{cx}) + y_r(x'_c k_{cy} - f_c i_{cy}) + z_r(x'_c k_{cz} - f_c i_{cz}) = x'_c(\boldsymbol{O_c} \cdot \boldsymbol{k_c}) - f_c(\boldsymbol{O_c} \cdot \boldsymbol{i_c}), \quad (6)$$

and

$$x_r(y'_c k_{cx} - f_c j_{cx}) + y_r(y'_c k_{cy} - f_c j_{cy}) + z_r(y'_c k_{cz} - f_c j_{cz}) = y'_c(\boldsymbol{O_c} \cdot \boldsymbol{k_c}) - f_c(\boldsymbol{O_c} \cdot \boldsymbol{j_c}). \quad (7)$$

There are identical relations for the projector image coordinates (x'_p, y'_p) and the real world coordinates (x_r, y_r, z_r) of the projected light on the object. The pinhole projector model also provides relations for the perspective projection in the projector coordinates (x_p, y_p, z_p) with origin $\boldsymbol{O_p}$:

$$x'_p = f_p \frac{x_p}{z_p} \quad (8)$$

$$y'_p = f_p \frac{y_p}{z_p}, \quad (9)$$

where f_p is the projector focal length. The position vectors from $\boldsymbol{O_p}$ to the projector image plane, $\boldsymbol{S'_p} = \overrightarrow{O_p S''} = \boldsymbol{S''} - \boldsymbol{O_p}$, and the object surface, $\boldsymbol{S_p} = \overrightarrow{O_p S} = \boldsymbol{S} - \boldsymbol{O_p}$, in terms of the perspective projection are related by:

$$\boldsymbol{S'_p} = \frac{f_p}{\boldsymbol{S_p} \cdot \boldsymbol{k_p}} \boldsymbol{S_p}, \quad (10)$$

Equations (8), (9), and (10) also provide a system of equations for the real coordinates:

$$x_r(x'_p k_{px} - f_p i_{px}) + y_r(x'_p k_{py} - f_p i_{py}) + z_r(x'_p k_{pz} - f_p i_{pz}) = x'_p(\boldsymbol{O_p} \cdot \boldsymbol{k_p}) - f_p(\boldsymbol{O_p} \cdot \boldsymbol{i_p}), \quad (11)$$

and

$$x_r(y'_p k_{px} - f'_p j_{px}) + y_r(y'_p k_{py} - f_p j_{py}) + z_r(y'_p k_{pz} - f'_p j_{pz}) = y'_p(\boldsymbol{O_p}\cdot\boldsymbol{k_p}) - f_p(\boldsymbol{O_p}\cdot\boldsymbol{j_p}), \quad (12)$$

where $\boldsymbol{i_p} = (i_{px}, i_{py}, i_{pz})$, $\boldsymbol{j_p} = (j_{px}, j_{py}, j_{pz})$, and $\boldsymbol{k_p} = (k_{px}, k_{py}, k_{pz})$ are the unit vectors in the two tangential directions and the normal direction to the projector focal plane. Finally, the matrix form of the system of equations for the real coordinates is

$$\boldsymbol{TX} = \boldsymbol{B}, \quad (13)$$

where

$$\boldsymbol{X} = \begin{pmatrix} x_r & y_r & z_r \end{pmatrix}^T \quad (14)$$

$$\boldsymbol{T} = \begin{pmatrix} x'_c k_{cx} - f_c i_{cx} & x'_c k_{cy} - f_c i_{cy} & x'_c k_{cz} - f_c i_{cz} \\ y'_c k_{cx} - f_c j_{cx} & y'_c k_{cy} - f_c j_{cy} & y'_c k_{cz} - f_c j_{cz} \\ x'_p k_{px} - f_p i_{px} & x'_p k_{py} - f_p i_{py} & x'_p k_{pz} - f_p i_{pz} \\ y'_p k_{px} - f_p j_{px} & y'_p k_{py} - f_p j_{py} & y'_p k_{pz} - f_p j_{pz} \end{pmatrix} \quad (15)$$

$$\boldsymbol{B} = \begin{pmatrix} x'_c(O_{cx}k_{cx} + O_{cy}k_{cy} + O_{cz}k_{cz}) - f_c(O_{cx}i_{cx} + O_{cy}i_{cy} + O_{cz}i_{cz}) \\ y'_c(O_{cx}k_{cx} + O_{cy}k_{cy} + O_{cz}k_{cz}) - f_c(O_{cx}j_{cx} + O_{cy}j_{cy} + O_{cz}j_{cz}) \\ x'_p(O_{px}k_{px} + O_{py}k_{py} + O_{pz}k_{pz}) - f_p(O_{px}i_{px} + O_{py}i_{py} + O_{pz}i_{pz}) \\ y'_p(O_{px}k_{px} + O_{py}k_{py} + O_{pz}k_{pz}) - f_p(O_{px}j_{px} + O_{py}j_{py} + O_{pz}j_{pz}) \end{pmatrix} \quad (16)$$

The projector image coordinates (x'_p, y'_p) of the color blocks, whose locations are prescribed by users, are known, while the camera image coordinates (x'_c, y'_c) for the locations of the color blocks illuminated on the surface can be estimated from the images. The real location $\boldsymbol{S}$ of the illuminated surface can be determined by solving the matrix Equation (13), provided the unit vectors on the image and projector planes, together with the corresponding focal lengths, are specified during a calibration procedure, which is explained below.

2.1. *Calibration*

The color block pattern is projected onto a calibration board having a square grid with 15-mm spacing, and both the calibration grid and the projected blocks are recorded on the board. The recording process is then repeated for the board translated under the same projector illumination. The normal unit vectors $\boldsymbol{k_c}$ and $\boldsymbol{k_p}$ are determined from this pair of images, which show the relative real coordinates for the color blocks projected along the optical axis.

At the same time, Equation (4) is rewritten as

$$x'_c = P_x f_c i_{cx} + P_y f_c i_{cy} + P_z f_c i_{cz}, \quad (17)$$

where the position vector $\boldsymbol{P}$ is expressed by

$$\boldsymbol{P} = (P_x, P_y, P_z) = \frac{\boldsymbol{S_c}}{\boldsymbol{S_c} \cdot \boldsymbol{k_c}} \tag{18}$$

$\boldsymbol{P}$ and x'_c are given by the real and image coordinates of each projected block on the calibration board.

Another geometric constraint for the orthogonal unit vectors on the image plane is

$$\boldsymbol{i_c} \cdot \boldsymbol{k_c} = i_{cx}k_{cx} + i_{cy}k_{cy} + i_{cz}k_{cz} = 0 \tag{19}$$

The unit vector $\boldsymbol{i_c}$ and focal length f_c for minimizing the squared error are obtained by solving the over-determined system of equations

$$\begin{pmatrix} \sum P_x^2 & \sum P_x P_y & \sum P_z P_x \\ \sum P_x P_y & \sum P_y^2 & \sum P_z P_x \\ \sum P_z P_x & \sum P_y P_z & \sum P_z^2 \\ k_{cx} & k_{cy} & k_{cz} \end{pmatrix} \begin{pmatrix} f_c i_{cx} \\ f_c i_{cy} \\ f_c i_{cz} \end{pmatrix} = \begin{pmatrix} \sum x_c P_x \\ \sum x_c P_y \\ \sum x_c P_z \\ 0 \end{pmatrix} \tag{20}$$

The same procedure applied to Equation (5) yields $\boldsymbol{j_c}$, and f_p, $\boldsymbol{i_p}$ and $\boldsymbol{j_p}$ can also be determined by applying the least-squares method to Equation (10) and the orthogonality condition for the unit vectors.

2.2. *Color detection*

In the experiments, a five-color (red, blue, green, cyan, magenta) block pattern (Fig. 2) is projected onto the object being measured (see also Fig. 4). The color blocks are arranged in unique color patterns for adjacent blocks, enabling us to specify any projected color block corresponding to a recorded block on the image.

In general, the color phase reflected on a surface may be altered from the initial projected color, owing to optical absorption connected with material-dependent wave numbers of light. In the present investigation, a *Lab* color transform is used for quantifying the visual color differences. The *Lab* color is designated to appropriate human vision, which is described in a color-opponent color space with a brightness layer *'L'*, chromaticity layers *'a'* (red/green opponent component) and *'b'*(blue/yellow component), based on nonlinearly compressed CIE XYZ color space coordinates. The initial choromaticity nearest to the imaged choromaticity in the *Lab* color space is defined as the original color detected in the image. The centroid of the detected color block was used as image coordinates of the block.

The accuracy of this technique has been verified via a test measurement of the shape of a concrete block, which is discussed in the Appendix.

3. Experiments

The new technique was applied to laboratory experiments on three-dimensional wave fields with diffraction and reflection around structures and also to breaking

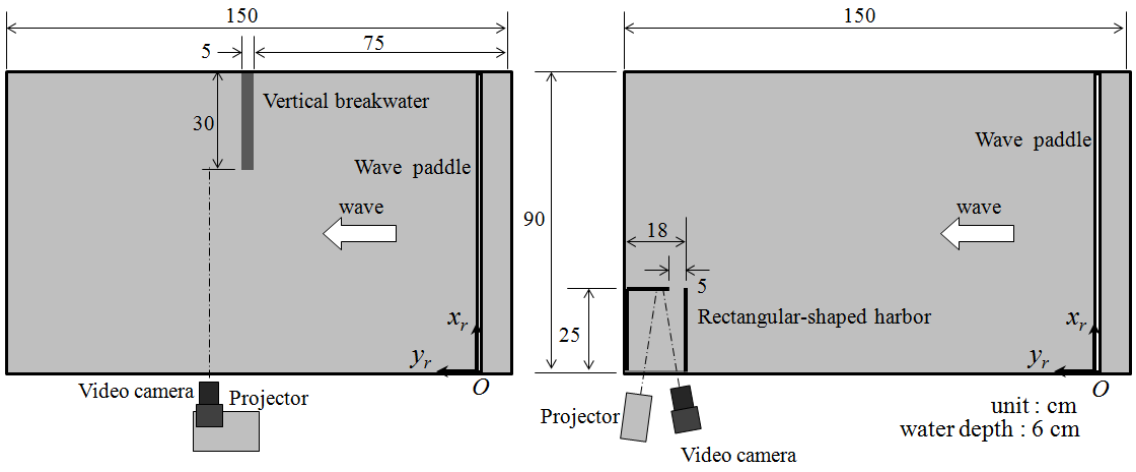

Fig. 3. Wave basins with a vertical breakwater (left) and with a rectangle-shaped harbor (right).

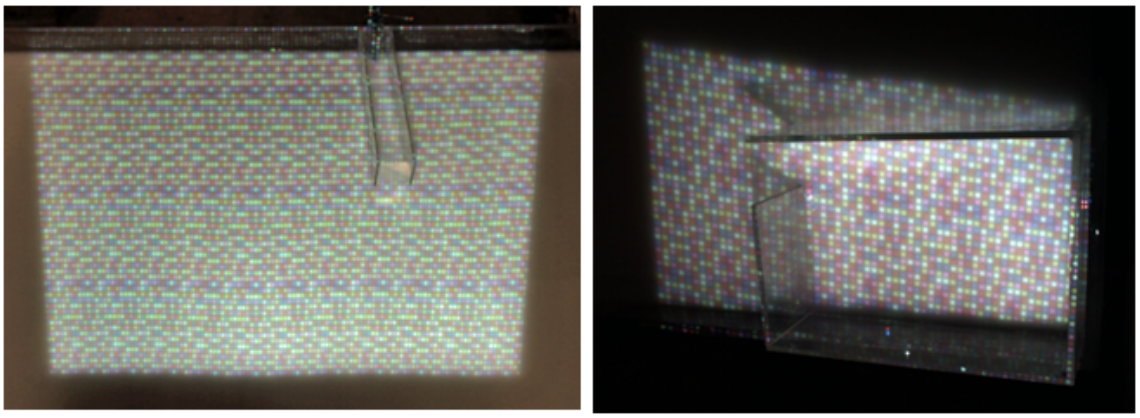

Fig. 4. Original images of illuminated surfaces around a breakwater (left) and a harbor (right).

waves over a uniform sloping beach. The experimental arrangements are described below.

3.1. *Wave field with structures*

A transparent acrylic wave basin, 150 cm in length, 90 cm in width, and 10 cm in height, was used for small-scale wave experiments on the wave field around a breakwater head and in a rectangular model harbor (see Fig. 3). In the first experiment, an acrylic board of length 30 cm and thickness 5 cm was installed adjacent to one of the side walls to receive incident waves normally, which induces typical diffracted waves in the lee of the board (see Fig. 3 left). In the second experiment, oscillations

of water surrounded by walls with a gap at one corner (a simple rectangular model harbor) were observed (see Fig. 3 right). A high-speed video camera (IDT, MotionScopeM3) and projector (Panasonic, PT-6000) were mounted beside the basin 45 cm above the still water level and focused on the water surface around the structures (see also Fig. 4). The optical axes of the camera and projector were angled vertically in the first experiment and horizontally in the second one to prevent the light from being blocked by the structures for each experiment. The resolution of the camera was 1280 × 1024 pixels, and the recording frequency was 60 Hz. Unidirectional periodic incident waves of height (H) 0.4 cm and period (T) 0.5 s were generated by a piston-type wave maker, and the uniform incident waves propagated at a fixed water depth h=6 cm in both experiments. The coordinates (x_r, y_r, z_r) are aligned with the direction of the wave crest, the direction of wave propagation, and the vertical direction, respectively (see Fig. 3). Alcoholic surfactants were used to reduce surface tension. White dye was dissolved in the water to scatter the projected light. Since maximum intensity of the scattered light from the dyed water is achieved at the location slightly below the surface, depending on dye concentration, the measured surface may also slightly deviate from a rigorous definition of free-surface. A dependency of the measured result on dye concentration should be examined in further research.

Since appropriate color detection was prevented at some locations, which were in the shadow of the walls or received multiple light reflections between structure walls and the surface (see Fig. 4), resulting spiky errors at these locations were removed through a median filtering operation.

Measured instantaneous planar distributions of the surface elevation were directly compared with the predictions of the Boussinesq equation model proposed by Madsen et al. (1991). The dimensionless grid spacing $\Delta x/h = 0.0833$, time step interval $\Delta t\sqrt{g/h} = 0.0064$, and the model coefficient B=1/21 were used in the computation.

Table 1. Wave conditions for breaking wave experiments.

RUN	Breaking wave height H_b (cm)	Breaking water depth h_b (cm)	Wave period T (s)	Bottom slope (cm)
1	11.0	11.8	2.0	1/20
2	8.0	11.8	1.0	1/20
3	13.8	14.8	1.43	1/17

3.2. *Breaking waves*

Breaking wave surfaces were measured in a wave flume 8 m in length, 0.25 m in width, and 0.4 m in depth (see Fig. 5). Periodic sinusoidal waves, generated by

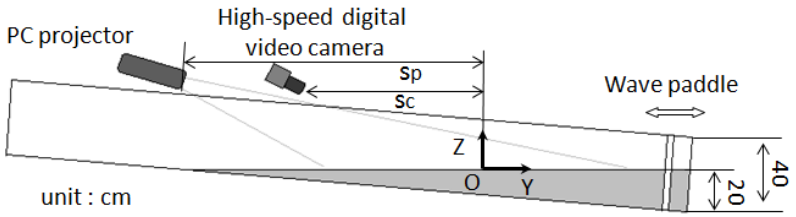

Fig. 5. Wave flume with uniform sloping bottom. Distances from the origin to the camera (S_c) and projector (S_p): S_c=64 cm, S_p=145 cm in case 1; S_c=108 cm, S_p=225 cm in case 2; S_c=34, S_p=150 cm in case 3.

a piston-type wave maker set up at one end of the flume, propagated on a uniformly sloping beach and finally broke at a depth h_b (see Table 1). The coordinates (x_r, y_r, z_r) are aligned with the lateral, offshore-ward, and vertical directions, with the origin located at the breaking point at the still water level (see Fig. 5). The same video camera and projector used in the first experiment were positioned above the wave flume to focus obliquely downward on the waves of dyed water in the post-breaking area. The water depth at the wave paddle was 20 cm. The recording frequency was 90 Hz.

The dynamic evolution of the breaking wave shapes was investigated for three incident wave conditions (see Table 1). Since the mean spacing of the projected color blocks was about 7 mm on the surfaces, surface fluctuations smaller than the block spacing (including air-bubbles and sprays) were unresolved in the experiments.

4. Results

4.1. *Wave field around the breakwater head*

The measured surface displacements in successive phases around the breakwater head are compared with the predicted values in Fig. 6. In both the measured and predicted results, the diffracted waves propagate radically in the shadow area. The lateral surface undulations near the breakwater along the direction of a wave crest are also consistent. Data are missing from some locations, which were in the shadow of the walls or received multiple light reflections between structure walls and the surface, and color detection was prevented at these locations. However, reasonable wave field measurements are confirmed except in these undetermined areas.

Measured time records of the surface elevation in two locations of the lee area, shown in Fig. 6, also correlate with the predictions (see Fig. 7), indicating the reliability of the present technique.

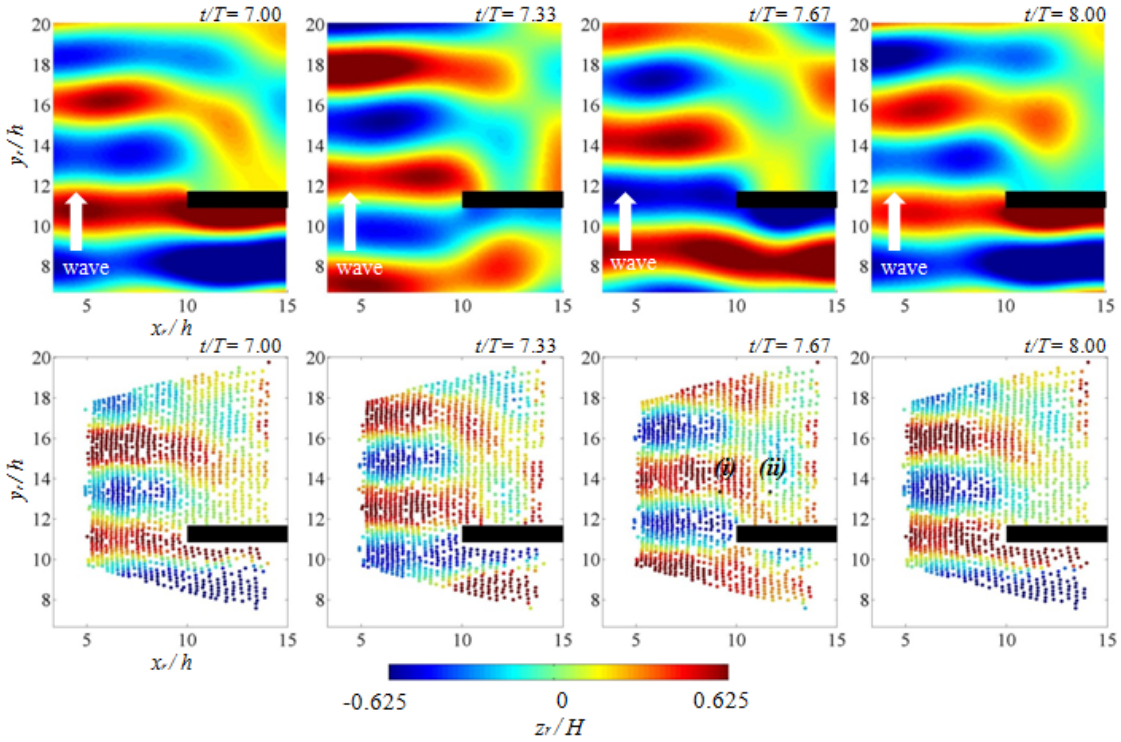

Fig. 6. The spatial distributions of the surface elevation around the breakwater head, computed by the Boussinesq equation model (top) and measured by the current technique (bottom). The time records at the locations (i) and (ii) in the third panel of the measured results are compared in Fig. 7.

4.2. *Wave field near the harbor mouth*

The same comparisons are made between the measured and predicted surface displacements near the rectangular harbor model, and the results are shown in Fig. 8. Since the illuminated colors on the surface were undetected in the shadow regions of the walls and also in the regions with multiple reflections between the walls and the surface (see also Fig. 4 right), there are many undetermined locations. However, the measurements and predictions coincide on the major features of the surface oscillations in the harbor caused by the propagation of diffracted waves. The reasonable correlations between the measured and predicted time records of the surface elevation at (i) the middle of the harbor and (ii) the harbor mouth, shown in Fig. 9 (see also locations (i) and (ii) in Fig. 8), also indicate the ability of the new technique to identify a three-dimensional wave field, provided there is no optical interference or interruption of the projected color blocks.

The root-mean-square differences between the measured and computed surface elevations shown in Fig. 7 and Fig. 9 were estimated to be 0.38 and 0.31 mm,

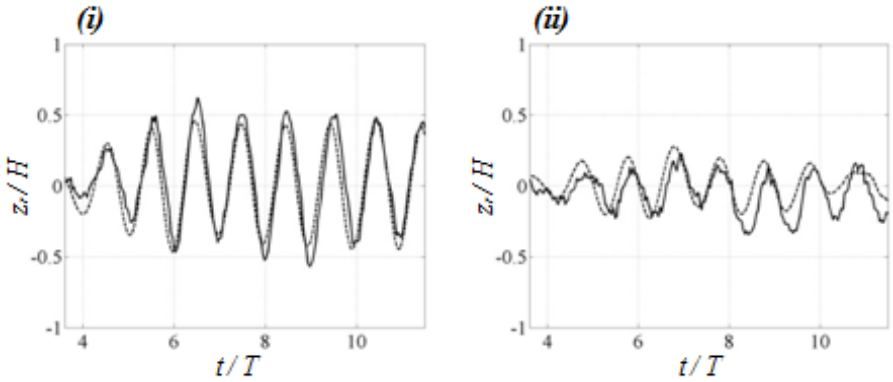

Fig. 7. Comparisons of the time records of the computed (dotted line) and measured (solid line) surface elevations at the open (i) and shadow (ii) regions in the lee of the breakwater. See the locations (i) and (ii) in the third panel of the measured results in Fig. 6.

respectively. They are less than the maximum error of 0.4 mm estimated in an accuracy test of the current technique, which will be explained in the Appendix.

4.3. *Breaking waves*

In the surf zone, the free surface of a breaking wave is rapidly transformed during propagation, which is conventionally characterized by the breaker type. For a plunging breaker, the splashing of the overturned wave crest on the forward surface creates large vortices beneath the wave surfaces during the splash-up cycle. Watanabe and Mori (2008) observed that the three-dimensional vortices under the broken waves entrain the surface into the inner fluid region to form so-called scars on the surfaces (see also Watanabe et al., 2005). The intensification of the subsurface vortices leads to the amplification of scars laterally arrayed on the jets, causing lateral disintegration of these scarified jets into so-called finger jets (Saruwatari, Watanabe, and Ingram, 2008).

The present technique is able to provide measurements of local transformations of a breaking wave surface that are consistent with these local splashing behaviors, including the formation of the overturning jet, the scarified surfaces behind the wave crest, and the secondary finger jets (see Fig. 10). Since there was no model structure to create optical interference in this experiment, most of the color blocks projected onto the surface were detected in the images, and hence the smooth surface plane was recomposed via Delaunay triangulation between the discrete, measured surface locations without any filtering operation.

The free-surface shapes for a spilling breaker take the form of a steep wave crest spilling down on the forward wave face (see Fig. 11). There are also scars in this case, extending longitudinally from the crest on the rear face of the wave, which is

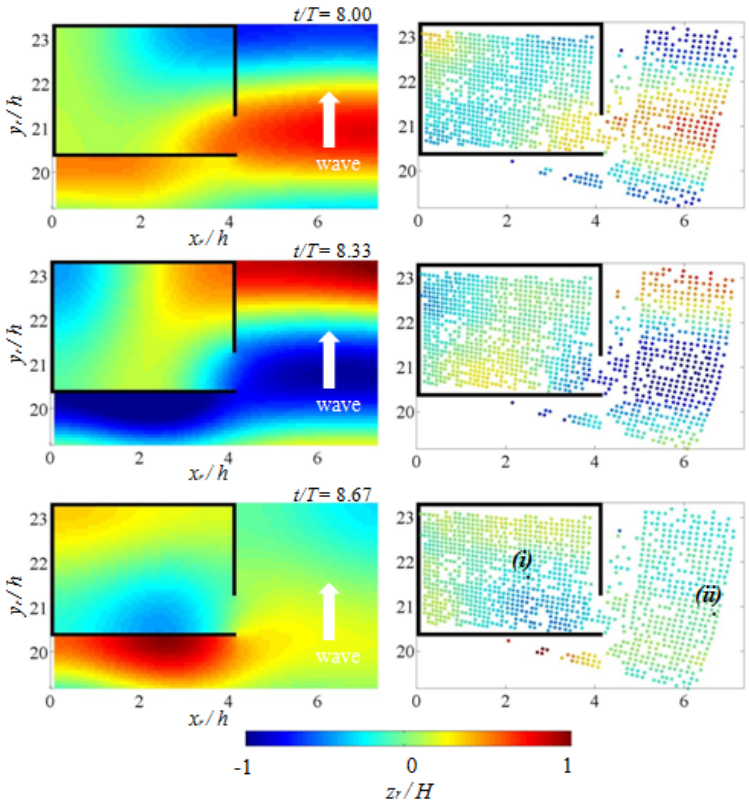

Fig. 8. The spatial distributions of the surface elevation around the model harbor mouth, computed by the Boussinesq equation model (left) and measured by the current technique (right). The time records at the locations (i) and (ii) in the third panel of the measured results are compared in Fig. 9

consistent with the major features observed by Watanabe and Mori (2008).

The side views of the surface shapes of the breaking waves in run 1 (Fig. 10c) and run 2 (Fig. 11c) are found to be identical with the video images of the respective surface profiles in the same phases (see Fig. 12), which also confirms the reliability of our method.

Fig. 13 shows the surface displacements of the plunging waves of run 3 after the plunging phase. Small fingers are initiated and laterally aligned at a certain interval of several centimeters during the early stage (see plan view (*b*) in Fig. 13at t=0.4 s after wave breaking). The fingers become thicker and merge with adjacent fingers during the splash-up process. Further research will be necessary to identify this transitional mechanism of the organized fingered surface during the wave-breaking process.

Since there has been no other research on three-dimensional surface measurement of breaking waves, the present technique may offer new insights into the fluid

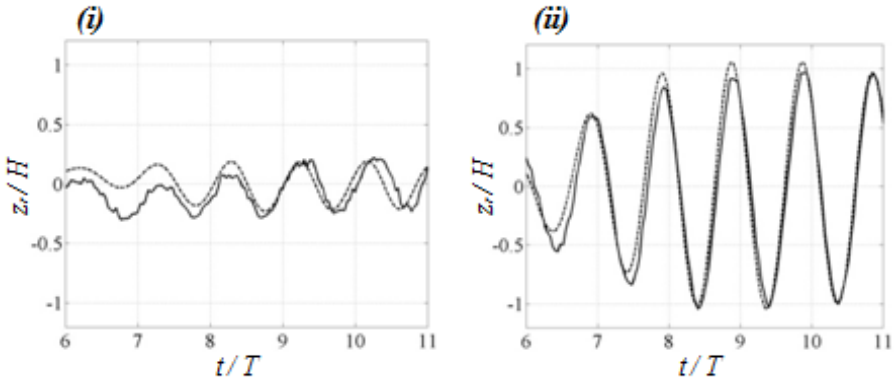

Fig. 9. Comparisons of the time records of the computed (dotted line) and measured (solid line) surface elevations at the middle (i) and mouth (ii) regions of the harbor mouth. See the locations (i) and (ii) in the third panel of the measured results in Fig. 8.

dynamics of the surf zone.

5. Conclusions

A novel imaging technique was proposed for identifying the locations of liquid surfaces, using a digital camera and PC projector. The procedure was applied to laboratory experiments for determining the spatial distribution of surface elevations around a structure in a wave basin, as well as the three-dimensional surface deformations produced after wave breaking.

Three-dimensional wave fields, consisting of superposed diffracted and reflected waves, were measured near a breakwater head and a harbor mouth in a wave basin, and the results coincided with the predictions of a conventional Boussinesq-type equation model, indicating the reliability of the new technique for quantifying wave surface elevation.

The procedure is capable of measuring the complex three-dimensional surface shapes that appear during the wave-breaking process, scarifying the surface behind the wave crests and fingering the splashing jets with features identical to those previously predicted by Saruwatari, Watanabe, and Ingram (2009).

Since there is no other existing procedure for quantifying local wave shapes in the laboratory surf zone, the present technique may contribute to future research on the identification of mechanisms that produce local surface undulations via turbulence.

A stereoscopic imaging method, which measures three-dimensional coordinates of corresponding points from a pair of images taken by two digital cameras, is often used for a surface measurement of solid object. Since correlation between intensity patterns of the images determines the corresponding points in this method, a measurement error generally depends on optical environment as well as surface patterns

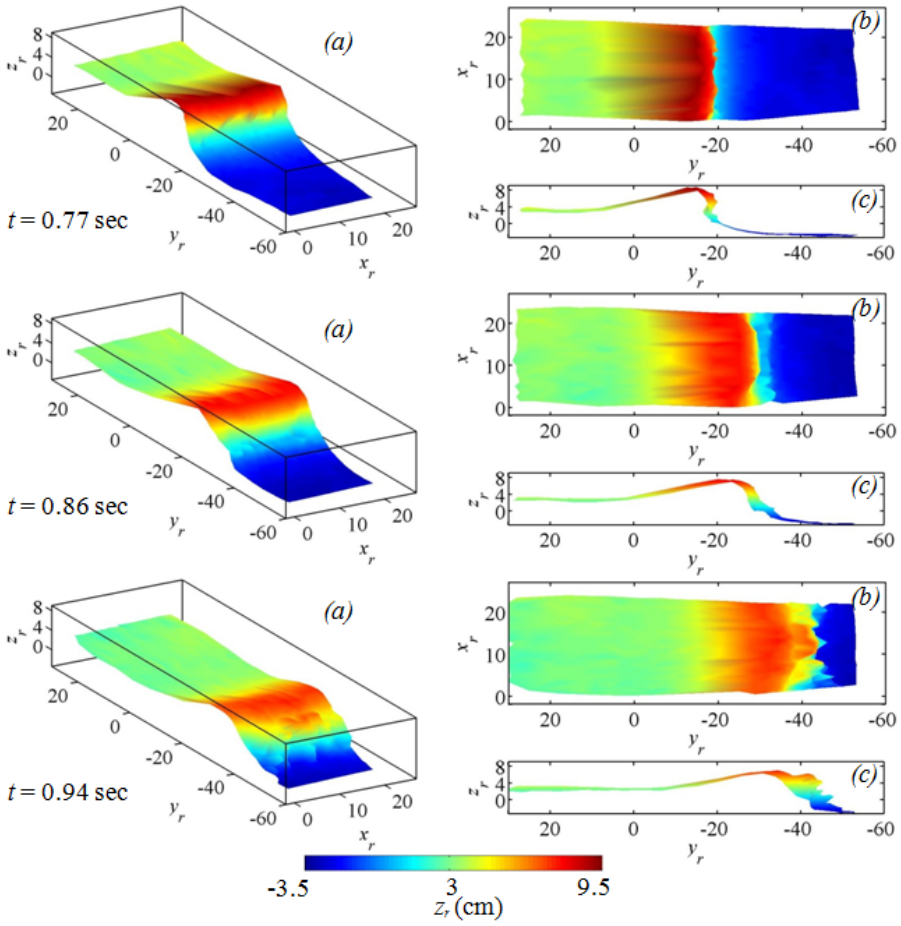

Fig. 10. Evolution of the surface shapes of plunging breaking waves (case 1): perspective view (a), plan view (b) and side view (c).

and material of the object. Because the measurement is unavailable for locations where is no variation of the image intensity, paint is often sprayed on the object surface to give additional intensity variations, which is generally inapplicable to liquid. The current technique, using projector illumination to link the corresponding color blocks on the projector and camera images, is advantageous to measure any location of both solid and liquid surfaces with less dependency on optical environment.

Acknowledgments

This research was partly supported by a Construction Technology Research Grant (No. 10), Ministry of Land, Infrastructure, Transport, and Tourism, Japan.

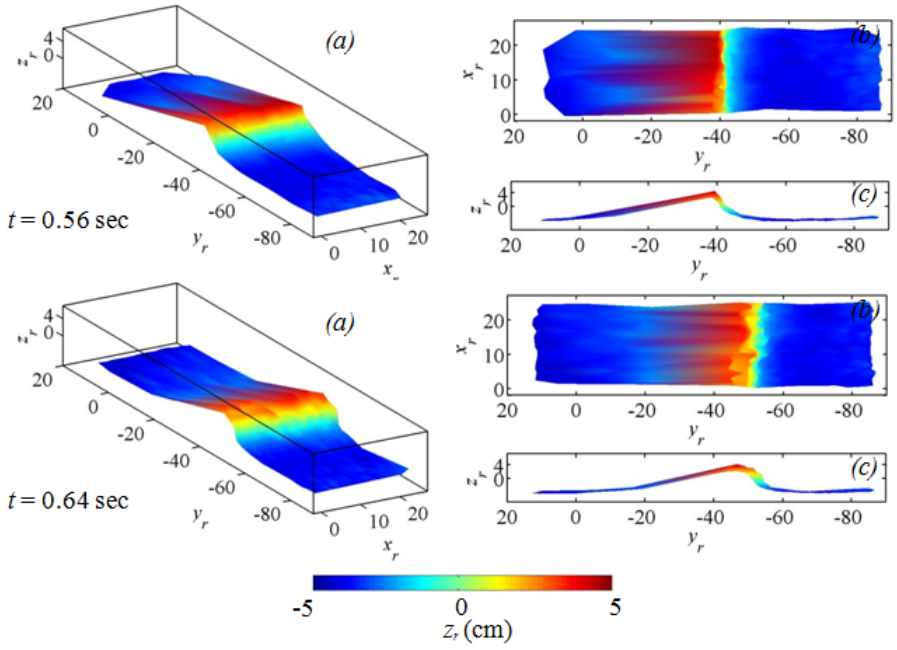

Fig. 11. Evolution of the surface shapes of spilling breaking waves (case 1): perspective view (a), plan view (b) and side view (c)

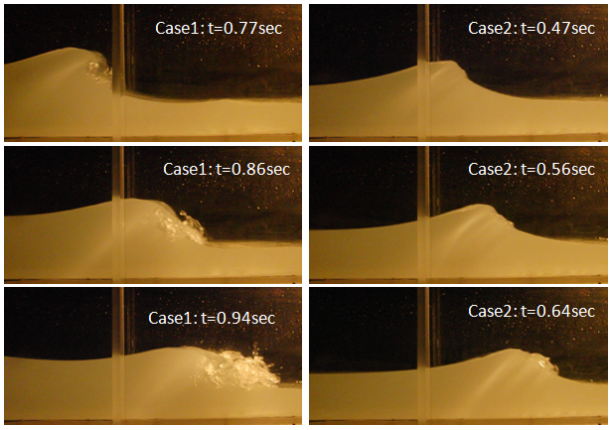

Fig. 12. Video images of the surface profiles of breaking waves; case 1 (left) and case 2 (right).

Appendix A. Measurement accuracy

The three-dimensional surface coordinates of a rectangular concrete block 10 cm in width, 6 cm in depth, and 20 cm in height were measured to estimate the accuracy of the new technique. The same digital camera and projector described in §3.1 were

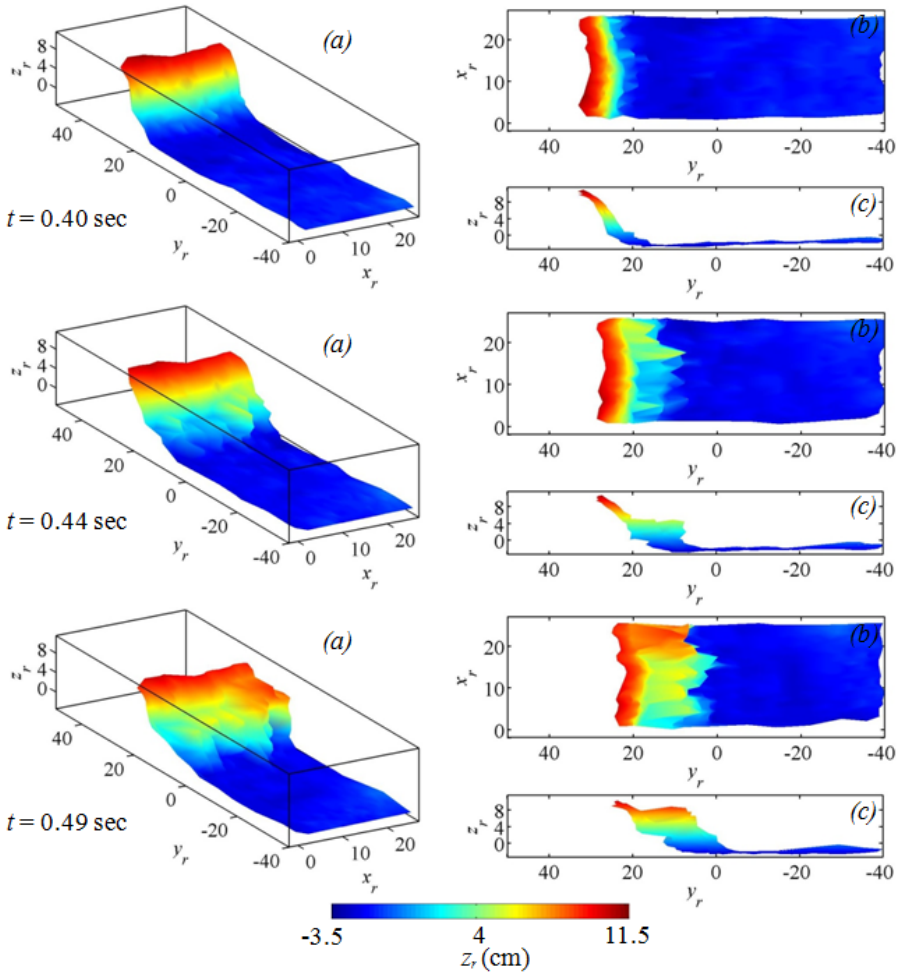

Fig. 13. Evolution of the surface shapes of plunging breaking waves (case 3): perspective view (a), plan view (b) and side view (c)

used in this test.

The color block pattern was directly projected onto the concrete block (see Fig. 14), and the measured three-dimensional location of the center of each color block was compared with the real dimensions (see Fig. 14 c,) The measurements were coincided with the real dimensions of the concrete block except near the edges, where the projected color blocks partially deviated from the body. The probability density function of the measurement errors (discrepancies between the measured and real dimensions) indicates a maximum probability at 0.09 mm and a maximum error of about 0.4 mm (see Fig. 14d), ensuring that the procedure has a reasonable degree of accuracy and reliability. It is reasonable to expect an identical degree of accuracy for the measurement of free-surface locations discussed in the body

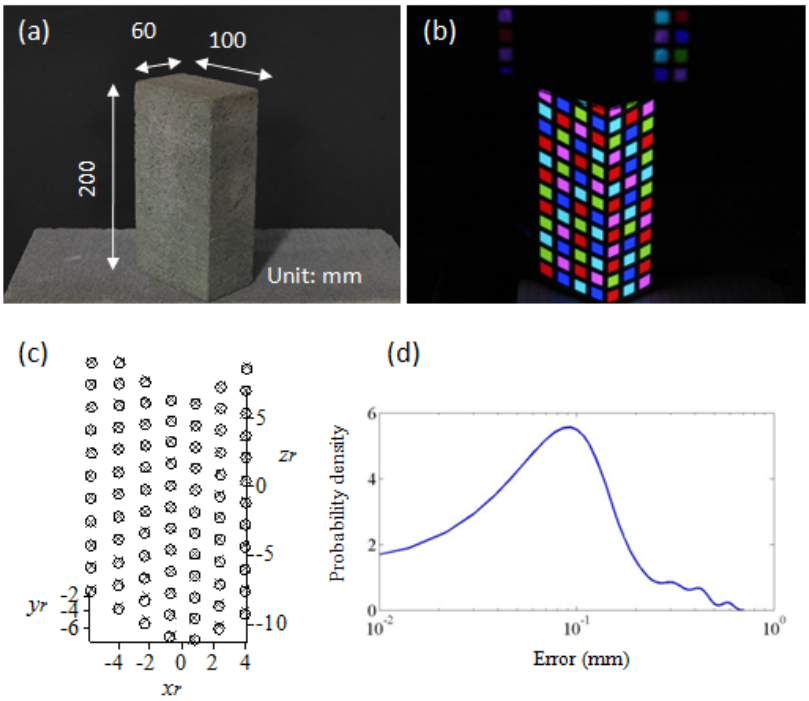

Fig. 14. Dimension of the concrete block (a), original image of the measurement (b, color blocks are projected to the object surface), comparison of the measured (∘) and real (×) locations of the object surface (c), and probability density of the measurement error (d).

of the paper because the object size for this test is of the same length scales as the model structures in §3.1 and the breaking wave heights listed in Table 1. In passing, since the projector light is perspectively expanded with distance between the projector and the object, a measurement error also linearly increases with the measurement distance. The maximum error has been confirmed to be less than 0.1% of the distance.

References

Brocchini, M. and Peregrine, D.H. 2001 The dynamics of strong turbulence at free surfaces. Part 1. Description *J. Fluid Mech.* **449**, pp. 225 – 254

Chen, S.Y. and Y.F. Li (2003). Self-recalibration of a color-encoded light system for automated three-dimensional measurements, *Meas. Sci. Thechnol.*,**14**, pp. 33 – 40.

Madsen, P.A., R. Murray and O.R. Sorensen (1991). A new form of the Boussinesq equation with improved linear dispersion characteristics, Part 1, A slowly-varying bathymetry, *Coastal Eng.*,**15**, pp. 371 – 388.

Saruwatari, A., Watanabe, Y. & Ingram, D. M., 2009. Scarifying and fingering surfaces of plunging jets. *Coastal Engineering*, **56**, pp. 1109–1122.

Watanabe, Y., Saeki, H. & Hosking, R. J., 2005. Three-dimensional vortex structures under breaking waves. *J. Fluid Mech.*, **545**, pp. 291–328.

Watanabe, Y., Mori, N., 2008. Infrared measurements of surface renewal and subsurface vortices in nearshore breaking waves. *J. Geophys. Res.*, **113**, C07015, doi:10.1029/2006JC003950.